Available online at www.sciencedirect.com
SCIENCE DIRECT®
ELSEVIER
Journal of Nuclear Materials 321 (2003) 221–232
journal of nuclear materials
www.elsevier.com/locate/jnucmat

Determination of the alloying content in the matrix of Zr alloys using synchrotron radiation microprobe X-ray fluorescence

A. Yilmazbayhan [a], O. Delaire [a], A.T. Motta [a,*], R.C. Birtcher [b], J.M. Maser [c], B. Lai [c]

[a] *Department of Mechanical and Nuclear Engineering, The Pennsylvania State University, 227 Reber Building, University Park, PA 16802-1400, USA*
[b] *Materials Science Division, Argonne National Laboratory, 9700 South Cass Ave., Argonne, IL 60439, USA*
[c] *Advanced Photon Source, Argonne National Laboratory, 9700 South Cass Ave., Argonne, IL 60439, USA*

Received 25 October 2002; accepted 29 April 2003

Abstract

The alloying element content in the α-Zr matrix of Zr alloys was studied using synchrotron radiation microprobe X-ray fluorescence, coupled with Monte Carlo simulation of the fluorescence process for quantification of the concentrations. The agreement between the measured values and the bulk concentrations of the alloy standards, as measured by the overall fit of the full fluorescence spectrum, was excellent. We measured the concentration of insoluble alloying elements in the matrix of Zircaloy-4 previously annealed to 705 °C for 125 h (corresponding to a cumulative annealing parameter (CAP) of 2.1×10^{-16} h, $\mathrm{CAP} = \sum_i t_i \exp(-Q/RT_i)$ where t_i is the time (hours) spent at temperature T_i (K) and $Q/R = 40\,000$ K) and in the matrix of a ZrSnNbFe alloy with a composition similar to ZIRLO™, but annealed at 710 °C for 92 h. The matrix concentrations of alloying elements were found to be, Fe = 290 wt. ppm, Cr = 270 wt. ppm in Zircaloy-4 and Fe = 250 wt. ppm in the ZrSnNbFe alloy. These results are discussed in light of other experimental determinations of alloying element concentrations in the literature.

1. Introduction

Zr alloys are used for fuel cladding tubes and core structural materials in water-cooled nuclear reactors. The microstructure of these alloys strongly influences their behavior under neutron irradiation, especially at high fuel burn-up [1]. In particular, the distribution of transition alloying elements (Fe, Cr) in the α-Zr solid solution has been linked to many aspects of alloy behavior such as the alloy corrosion resistance [2–5] and the rate of irradiation growth [6]. Although iron is only a minor alloying element in Zircaloy-4 and in other alloys, there is evidence that when in solution it influences high temperature mass transport [7,8] as well as irradiation damage [9] and corrosion [10,11]. Furthermore, the alloying elements that are not in the alpha matrix are precipitated out, and the size and distribution of second phase particles are also a factor in determining corrosion resistance [12,13]. Thus, it is of great scientific and technological interest to determine the concentration of alloying elements in the matrix of Zr alloys and the exact partitioning of these elements in the alloy between the matrix and precipitates.

Numerous techniques are available to analyze compositions of samples or obtain spatial distribution of elements, but very few allow the quantitative determination of the concentration of trace elements on a

* Corresponding author. Tel.: +1-814 865 0036; fax: +1-814 863 4848.
E-mail address: atm2@psu.edu (A.T. Motta).

0022-3115/$ - see front matter © 2003 Elsevier B.V. All rights reserved.
doi:10.1016/S0022-3115(03)00267-8

microscopic basis. For example, with common conventional energy dispersive spectroscopy (EDS) used in transmission electron microscopes (TEM) it is possible to examine a spot as small as 2 nm, but this technique cannot detect the very low levels of Fe and Cr found in the matrix of Zr alloys [14]. Other studies using different techniques have attempted to measure the concentration of transition elements in the matrix of Zircaloy and other Zr alloys [15–21] but the results show a significant degree of variability, possibly reflecting also the variability in the samples utilized in each study.

In this work we measure the concentrations of the alloying elements in the matrix of the Zr-based alloys, using an X-ray microprobe [22,23] at the Advanced Photon Source facility at Argonne National Laboratory (ANL). When paired with the use of synchrotron radiation (SR), microprobe X-ray fluorescence (μ-XRF) has a unique combination of spatial resolution and elemental sensitivity [14,24,25]. In third generation synchrotron storage rings, it is possible in a matter of minutes to obtain fluorescence spectra with sensitivity in the parts per million, from a region as small as 0.05 μm^2. We discuss the results obtained in light of previous experiments.

2. Experimental methods

2.1. Sample preparation

Table 1 gives the concentrations (and the elemental detection limits) of the different alloys examined in this work, as measured by direct current plasma emission spectroscopy (E1097-97 Standard Guide for Direct Current Plasma Emission Spectrometry Analysis, ASTM International). Zircaloy-4 samples were obtained from General Electric Corporation as plate material. ZIRLO™ (ZrSnNbFe) samples were obtained from Westinghouse Electric Company, LLC, as tube material. The material for the pure Zr standard was obtained from Goodfellow Corporation (here called 'nominally pure Zr'). The nominally pure material has a measured Fe concentration of 310 wt. ppm.

The Zircaloy-4 and ZrSnNbFe samples were annealed in a quartz tube filled with ultra-high purity Ar for ten minutes at 1050 °C to completely dissolve the precipitates and put the alloying elements back into solution in the beta-phase matrix. After the heat treatment, the samples were rapidly quenched by breaking the quartz tube over a bucket of water. A small amount of discoloration in these samples resulting from the high temperature treatment and quench was removed by further mechanical polishing. The Zircaloy-4 samples were re-sealed into quartz tubes and annealed at 705 °C for 125 h, which corresponds to a cumulative annealing parameter (CAP) of 2.1×10^{-16} h.

The CAP is defined as [26]

$$\mathrm{CAP} = \sum_i t_i \exp(-Q/RT_i), \tag{1}$$

where t_i is the time (hours) spent at temperature T_i (K) and $Q/R = 40\,000$ K.

The ZrSnNbFe samples were annealed at 710 °C for 92 h. Since the precipitate density in the as-furnished alloy was too high to allow easy measurement of the matrix content, we submitted the alloy to an annealing heat treatment designed to grow precipitates and decrease precipitate density. Because this heat treatment is

Table 1
Bulk compositions for Zircaloy-4, ZIRLO™ (ZrSnNbFe) and nominally pure Zr measured using direct current plasma emission spectroscopy

Element	Zircaloy-4 (wt. ppm)	ZrSnNbFe (wt. ppm)	Nominally pure Zr (wt. ppm)	Detection limit (wt. ppm)
Iron	2400	1070	310	5
Chromium	1130	10	160	5
Niobium	–	12 300	110	10
Tin	16 400	10 800	2700	10
Oxygen	1120	1450	1410	10
Zirconium	Balance	Balance	Balance	
Aluminum	58	120	<5	5
Carbon	30	20	440	10
Copper	20	20	36	5
Hafnium	<40	<40	<40	40
Manganese	<10	<10	<10	10
Molybdenum	<10	<10	<10	10
Nickel	34	<10	190	10
Nitrogen	20	50	90	10
Silicon	95	130	60	10
Titanium	12	19	<10	10
Tungsten	<40	<40	<40	40

very different from that used in the fabrication of the commercial alloy, the microstructure was different from that of ZIRLO despite the similar chemical composition. Both beta Zr and the omega phase appeared in TEM examination of the annealed ZrSnNbFe sample. Thus, the Fe concentration measured in the matrix could vary significantly from that in the commercial alloy.

The samples used in X-ray fluorescence measurements of matrix content were standard TEM thin foils (about 100 nm thick in their thinnest region) prepared from strips of the alloys. We used TEM foils to minimize the problem of 'buried' precipitates contributing to our counts. These foils were prepared by mechanically grinding the strips to a thickness of approximately 100 μm, punching out 3 mm diameter disks, then electropolishing in a solution of 670 ml methanol, 100 ml of butoxyethanol and 130 ml HCl, at a temperature of −60 °C and an electropolishing current of 20 mA. These samples were examined in a Philips CM-30 TEM at Argonne National Laboratory and in a Hitachi FE 2000 at Penn State.

2.2. Synchrotron beamline setup

Experiments were conducted at the 2-ID-D and 2-ID-E beamline at the Advanced Photon Source, which are operated by the Synchrotron Radiation and Instrumentation Collaborative Access Team (SRI-CAT). Fig. 1 shows a schematic of the hard X-ray microprobes at sector 2. An X-ray beam with an energy of 9 keV is focused on the specimen using a tunable Fresnel zone plate, creating excited atomic states in a small specimen volume. X-ray fluorescence photons emitted by the excited atoms are collected in an energy-dispersive detector. A raster-scan of the focused scan is executed across the specimen, and the X-ray fluorescence spectra recorded for each pixel. The X-ray beam is focused on the specimen by scanning a Cr knife edge through the focused beam, and recording the Cr fluorescence signal. Consecutive knife edge scans are executed for different specimen-zone plate distances to find the focal position with minimum spot size. Using this procedure, the X-ray beam was focused on the specimen and the full-width at half maximum (FWHM) of the beam in both x and y directions determined. For the present experiments, the beam size was determined to be 0.3×0.5 μm, except for the nominally pure Zr measurement for which the beam size was 0.5×0.8 μm.

We located the hole in the TEM foils by scanning across the sample to find the thinnest region (region with no fluorescence yield). Detailed X-ray fluorescence maps (10×10 μm) were acquired near the hole, with a step size of 0.5 μm or smaller. The energy dispersive Ge detector had an energy resolution of 200 eV. We typically examined regions located about 10 μm from the edge of the hole. Once a precipitate-free region was found, a higher resolution 2D fluorescence map was collected. The 2D map reveals precipitates and matrix regions, which can then be investigated by collecting fluorescence spectra at particular spots. To provide good statistics, the spectra collected from the matrix were taken for a minimum of 600 s and in most cases 1000 s or more.

3. Experimental results

3.1. Transmission electron microscopy

The quenched materials (Zircaloy-4 and ZrSnNbFe) showed a typical basket weave structure, characteristic of rapid cooling [14]. Detailed examinations with energy dispersive X-ray spectroscopy revealed no precipitates and showed no enrichment of alloying elements anywhere

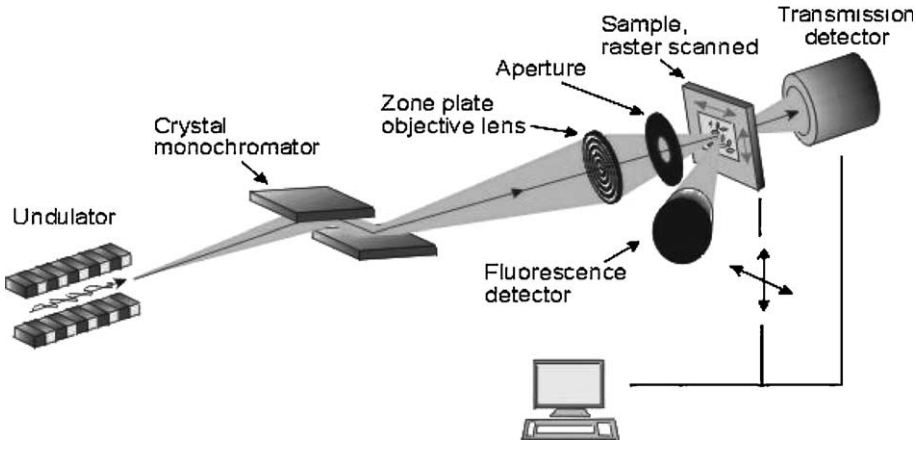

Fig. 1. Schematic depiction of experimental setup.

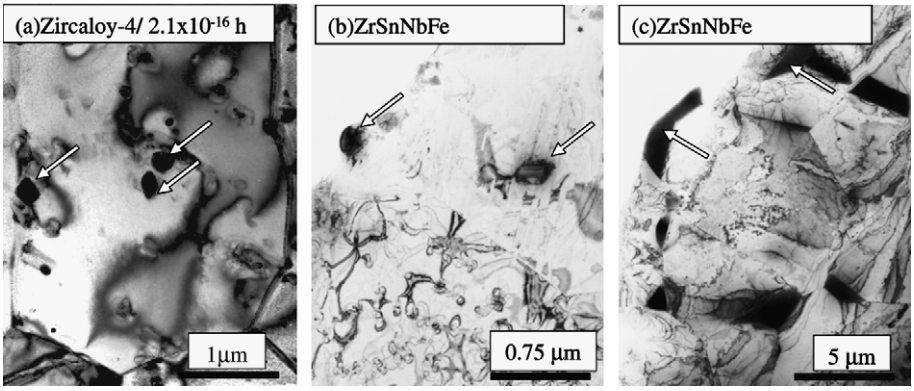

Fig. 2. TEM micrographs showing the microstructure of the alloys studied. In each case the arrows indicate: (a) $Zr(Cr,Fe)_2$ intermetallic precipitates in Zircaloy-4 after $CAP = 2.1 \times 10^{-16}$ h, (b) Zr–Nb–Fe intermetallic precipitates in the microstructure of annealed ZrSnNbFe and (c) β-Zr clusters with ω precipitates in the microstructure of annealed ZrSnNbFe.

in the structure, at least to the detection limit of the technique.

Fig. 2(a) is a bright-field TEM micrograph showing a typical recrystallized microstructure of annealed Zircaloy-4 ($CAP = 2.1 \times 10^{-16}$ h). The microstructure of Zircaloy-4 showed large grain sizes, low dislocation density, and the usual distribution of intermetallic particles of the type $Zr(Cr,Fe)_2$. The precipitate sizes were in the range of 0.1–0.3 μm. As can be seen from Fig. 2(a), these precipitates were, typically, several microns apart.

The ZrSnNbFe sample prior to quenching and high temperature annealing exhibited two types of precipitates [27]: small roundish Zr–Nb precipitates and Zr–Nb–Fe precipitates which have been recently identified as having the same crystal structure as the precipitates in Zircaloy-4 (C14 hcp $MgZn_2$ type Laves phase) [28]. After quenching and annealing, the microstructure of the ZrSnNbFe alloy exhibited Zr–Nb–Fe precipitates and large clusters of β-Zr with ω precipitation [29] (Fig. 2(b) and (c)). The Zr–Nb–Fe precipitate sizes were in the range of 0.2–0.4 μm. The β-Zr with ω precipitates was observed mostly in the triple points of the grain boundaries. They ranged in size from 1 to 1.5 μm and had triangular or rectangular shapes. Energy dispersive X-ray spectroscopy shows that β-Zr particles contain Nb and Fe. Given the different microstructure resulting from this different heat treatment, the amount of Fe in the α-Zr in this alloy after heat treatment is likely different than in standard ZIRLO.

3.2. Measurement of standards

In order to perform quantitative analysis, it is necessary to use standards. Fig. 3 shows several fluorescence spectra (in log scale) acquired using the SR μ-XRF

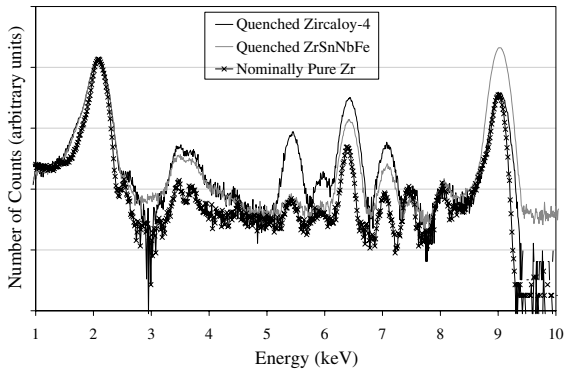

Fig. 3. X-ray fluorescence spectra obtained in different samples of quenched standards (logarithmic scale for number of counts).

from the three standards we chose: (i) quenched Zircaloy-4, (ii) quenched ZrSnNbFe, and (iii) nominally pure Zr sample (all in the form of TEM foils). In these samples, the concentrations should be close to those obtained from the overall bulk measurements of the alloy shown in Table 1. For the TEM thin foil samples, the fluorescence spectra were acquired from their thin region, in the same manner as in the samples of interest. The spectra are normalized to the integrated counts of Zr L peak to compensate for differences in acquisition times and thickness. Fig. 3 clearly shows that, in the standards, the magnitude of the fluorescence peaks associated with alloying elements increases with increasing alloying element content. These spectra are analyzed in the next section to provide a quantitative estimate of the concentrations.

To enable the acquisition of spectra from the *matrix* region in annealed Zircaloy-4 and ZrSnNbFe, large 2D

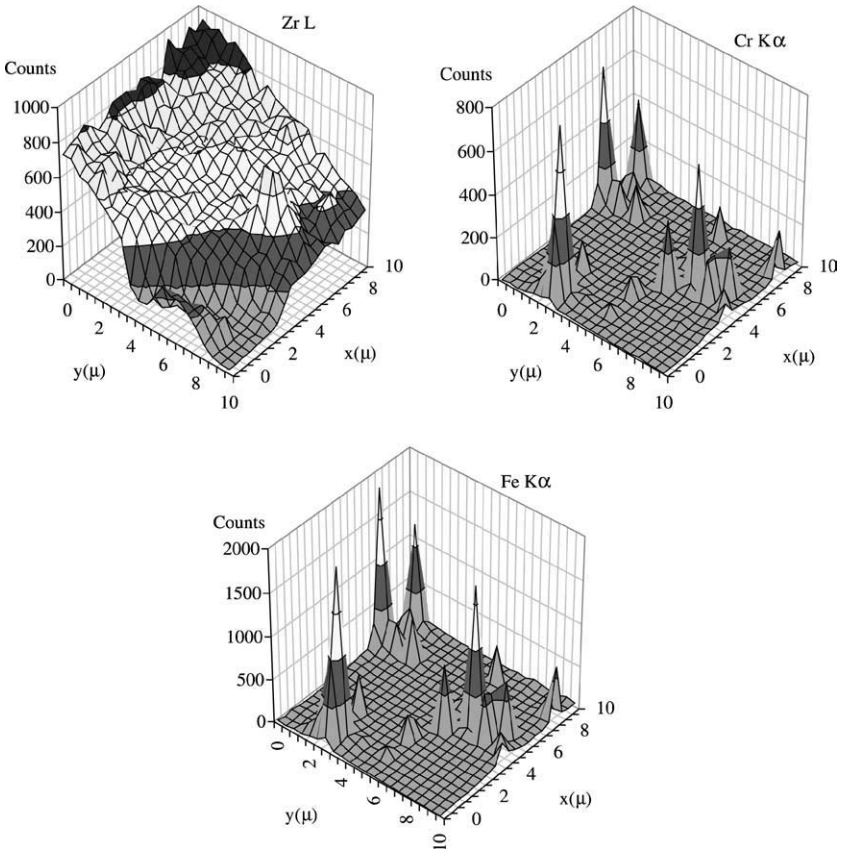

Fig. 4. X-ray fluorescence maps of Zr, Cr and Fe obtained in heat-treated Zircaloy-4 (10×10 μm, using step size of 0.5 μm).

fluorescence maps were acquired to identify the location of second phase particles and the matrix. Fig. 4 shows a 10×10 μm fluorescence intensity map of three different elements acquired using a 0.5 μm step size in annealed Zircaloy-4. A region with low intensity in Cr and Fe was identified from the large fluorescence map and examined using a finer scale map. This smaller map covers an area of 2×2 μm^2 with a step size of 0.2 μm and an acquisition time of 10 s per point. Fig. 5 shows four fluorescence intensity maps acquired on a recrystallized Zircaloy-4 sample on one such location. The Fe and Cr maps show peaks located at the same positions on both maps, which allows us to identify precipitates. The Zr and Sn maps present a smooth intensity, with a small gradient, caused by the thickness variation of the TEM foil.

Fig. 6(a), again in log scale, shows both a spectrum acquired from a quenched Zircaloy-4 sample and a spectrum acquired from the point indicated in Fig. 5 representing the matrix in a Zircaloy-4 sample. Spectra are normalized to Sn L peaks, since Sn is homogeneously distributed in the matrix of the alloy. The normalization procedure accounts for differences in signal intensity changes, in beam intensity and small sample thickness variations. Fig. 6(b) shows spectra acquired from the quenched ZrSnNbFe sample and from the matrix of the ZrSnNbFe alloy after heat treatment (from an equivalent alpha-Zr matrix site in the ZrSnNbFe sample as that shown in Fig. 5). It is clear from Fig. 6 that the matrix content is much lower in the heat-treated sample than in the quenched sample, but it is also clear that the alloying content in the matrix can be clearly distinguished with the synchrotron beam.

Although we did not determine precisely the detection limit of this technique, we can estimate it using our measurements performed on standards. We acquired a fluorescence spectrum in ultra-pure Zr, which was measured by Hood et al. [30] to have about 0.3 wt. ppm Fe; this spectrum showed no discernible Fe peak. In contrast, chemical analysis of the ZrSnNbFe alloy shows 10 wt. ppm Cr; a fluorescence spectrum acquired from the quenched version of this sample shows a discernible Cr peak (Fig. 6(b)), which rises above the background by about 10 wt. ppm. Cr, according to Monte Carlo calculations. This suggests that in the Fe/Cr region (6–7 keV) the detection limit lies between 0.3 and 10 wt. ppm.

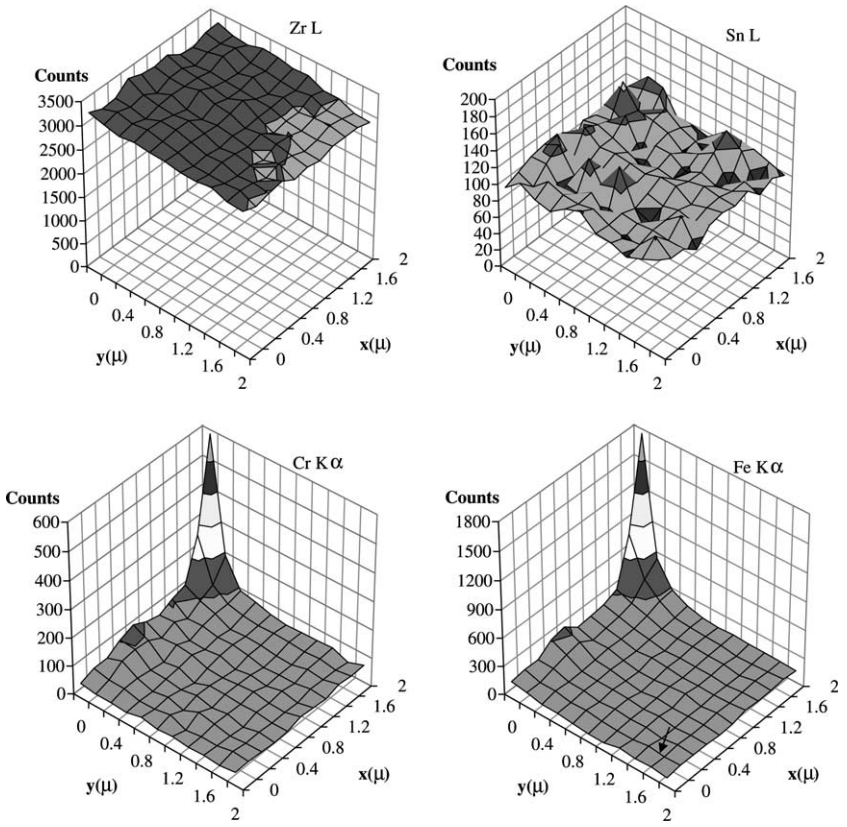

Fig. 5. X-ray fluorescence maps of Zr, Cr and Fe obtained in heat-treated Zircaloy-4.

3.3. Experimental analysis

3.3.1. Experimental biasing

To perform a measurement of alloying concentration in the matrix we have to ensure that we are in fact probing the matrix, and not second-phase particles. The procedure outlined above ensures that the beam is placed close to the hole and at the region of lowest Fe and Cr counts in the map. By placing the beam close to the hole we minimize the problem of extraneous contributions to the matrix counts from unseen (buried) precipitates. The average inter-precipitate distance is more than 1 μm in an alloy with a precipitate number density of 0.7×10^{12} cm^{-3} as is the case in the Zircaloy-4 sample used in this study (see also Fig. 2).

To evaluate the probability that the beam hits an undetected precipitate we performed a simple geometrical calculation [24]. This calculation considers a cylindrical X-ray beam impinging on a slab-shaped sample at an angle α. The sample contains N spherical precipitates of a single size, uniformly distributed per unit volume. The fluorescence detector can collect X-rays coming out of the sample between certain angles. To obtain a 'true' count of the alloying element content the sampled volume needs to be free of second-phase particles.

Fig. 7 shows the results of these calculations for Zircaloy-4. We assumed that all but 40 wt. ppm of Fe and 40 wt. ppm of Cr are in the form of precipitates of the stoichiometry $Zr(Cr_x,Fe_{1-x})_2$, with $x = 0.33$; from this we calculated the precipitate density by assuming that all the precipitates have the average precipitate size. For a 100 nm thick TEM foil such as used in this work, and a 0.3×0.5 μm beam size, and evenly distributed 250 nm diameter precipitates, the calculated precipitate density is 0.7×10^{12} cm^{-3}, and the probability of not hitting an unseen precipitate is 0.95. If the precipitate diameter is 140 nm, the precipitate density is 4×10^{12} cm^{-3} and the probability of not striking a precipitate in a random location is 0.85. These calculated probabilities assume *random* sampling of the alloy microstructure. Our location, however, was anything but random; in fact it was carefully chosen, using the 2D concentration measurement map, to minimize the probability that precipitates would be hit, so that the actual value of P in our experiments is likely higher than shown in Fig. 7.

If our beam were much smaller than the size of the precipitates, such that a sampling of the precipitates and

the matrix yielded a true ratio of fluoresced intensities, the ratio would be about *1000* for a matrix concentration of 330 at. ppm and *10 000* for a matrix concentration of 33 at. ppm (compared to 330 000 ppm in the precipitates). The actual ratio observed was actually about *30*. This is because the minimum concentration of alloying elements experimentally detected is higher than the matrix alloying element concentration. This range between the minimum detected concentration and the concentration of the matrix allows for small precipitates to remain undetected in fluorescence maps. Thus, there exists a precipitate size below which they cannot be detected if the minimum detectable limit (MDL) for the acquisition time used is higher than the matrix concentration. The critical size for detection is given by

$$\phi_{\text{crit}} = \phi_{\text{avg}} \left[\frac{I_{\text{avg}}}{I_{\text{bkgd}}} \right]^{-1/3}, \tag{2}$$

where I_{avg} is the number of counts when the beam is placed on a precipitate (average between precipitate and matrix) and I_{bkgd} is the number of counts when the beam is placed on the matrix. The ratio of Fe counts between the situation when the beam is placed on a precipitate and when it is placed on the matrix is approximately 30, because the beam size is normally larger than the precipitate size, and thus $I_{\text{avg}}/I_{\text{bkgd}}$ is $\sim$30.

This allows us to obtain a more precise estimate of the probability of biasing caused by undetected precipitates, by assuming we can avoid the big precipitates. Gros and Wadier [26] measured the precipitate size distribution in Zircaloy-4 after a very similar heat treatment schedule as ours (700 °C for 150 h, or CAP $= 2.1 \times 10^{-16}$ h) finding that the average particle diameter is 250 nm. Using Eq. (2) for $\phi_{\text{avg}} = 250$ nm and $I_{\text{avg}}/I_{\text{bkgd}} = 30$ yields $\phi_{\text{crit}} = 80$ nm. In the same work, the density of particles below 80 nm is 10^9 cm^{-3}, which translates into a random interaction between the beam

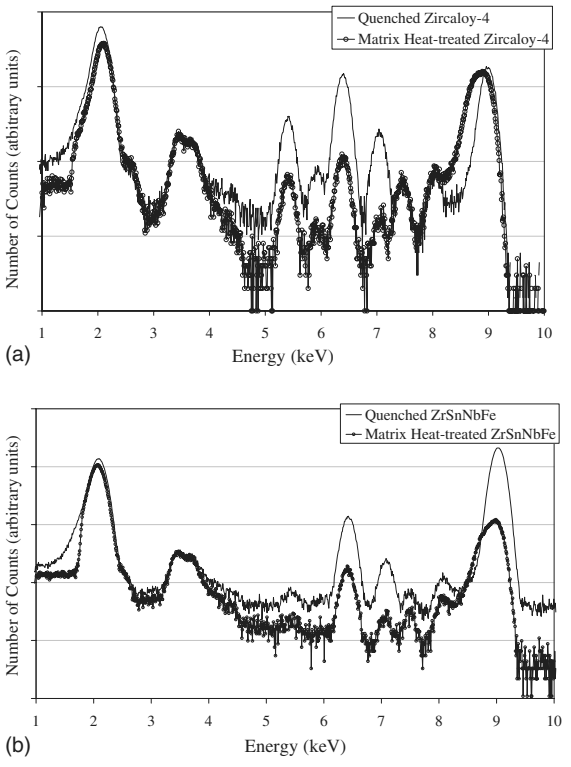

Fig. 6. X-ray fluorescence spectra obtained from (a) quenched Zircaloy-4 standard and heat-treated Zircaloy-4 thin foils and (b) quenched ZrSnNbFe standard and heat-treated ZrNbSnFe thin foils.

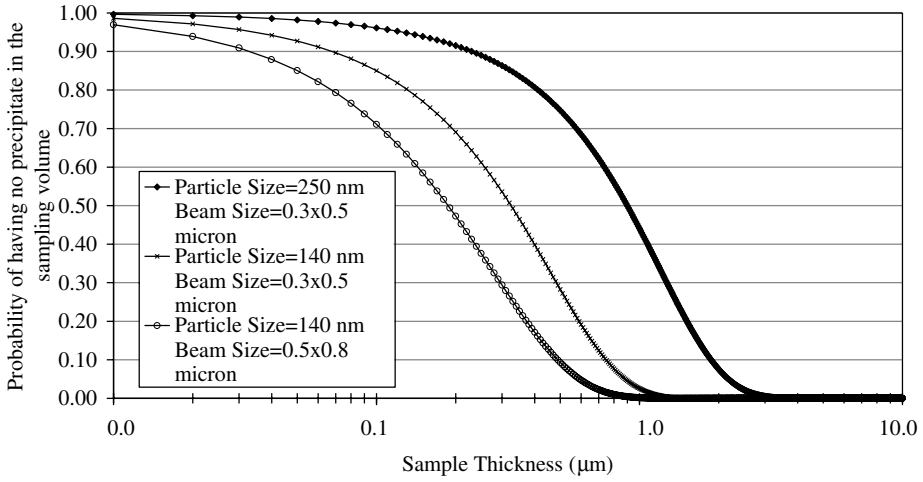

Fig. 7. Probability of having no precipitate in the beam sampling volume for a random distribution of particles of the specified diameter versus sample thickness.

and undetected precipitates of 4.2×10^{-5}, or to a probability of not hitting a precipitate of 99.996%. Thus, we conclude that no significant biasing of the matrix counts by unseen precipitates occurred in this work.

3.3.2. Quantitative analysis

The spectra acquired from quenched and heat-treated Zircaloy-4 and ZrSnNbFe alloys are analyzed in two different ways. To convert the measured number of counts into a concentration, we performed both a standard-based linear (Cliff-Lorimer) analysis and using a Monte Carlo simulation of the fluorescence profiles.

Linear analysis: In the linear analysis, the calculations are performed using the assumption that the samples were thin enough for the X-ray fluorescence count rate to vary linearly with the sample thickness. In this linear regime, the differences in sample thickness and also in incident beam intensity and acquisition time can be accounted for by simply equating the intensity coming from an element of known concentration to some arbitrary value proportional to its concentration.

The ratio of the concentration of a given element Z measured in the sample of interest and in a standard is equal to the ratio of integrated counts from some transition associated with element Z (e.g. K_α, K_β) in the fluorescence spectra from the two specimens. Since one knows the alloying content in the standard W_Z^{std}, the content in the sample, W_Z is given by

$$W_Z = W_Z^{\text{std}} \frac{N_Z}{N_Z^{\text{std}}}, \tag{3}$$

where N_Z is the number of counts for the transition considered of element Z in the sample and N_Z^{std} is the similar quantity for the standard.

Using this formula, we generated Table 2, which shows the concentrations of alloying elements for the different samples examined, using quenched Zircaloy-4 as a standard (values shown in bold were assumed and the others derived). The calculated concentrations of the other standards (quenched ZrSnNbFe and nominally pure Zr) are reproduced quite well.

Table 2
Calculated concentrations (wt. ppm) of Fe and Cr in quenched standards and in the matrix of heat-treated the Zircaloy-4 and ZrSnNbFe alloys

	Linear analysis		MC simulation	
	Fe Kα	Cr Kα	Fe Kα	Cr Kα
Standards				
Zircaloy-4	**2400**	**1130**	2400	1130
ZrSnNbFe	1052	131	1070	80
Nominally pure Zr	390	112	330	130
Alloys				
Zircaloy-4	320	307	290	270
ZrSnNbFe	174	56	250	70

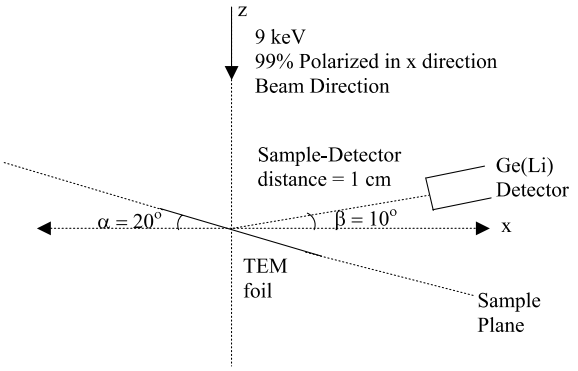

Fig. 8. Geometry of experimental setup, as modeled by the Monte Carlo program MSIM 5d.

Monte Carlo simulation: We also used a Monte Carlo simulation program to quantify the concentrations. By comparing the results of the simulation to the experimental data, it is possible to calculate the sample concentration. In order to simulate this μ-XRF experiment, we used the computer code MSIM 5d [31–33].

The geometry modeled is illustrated in Fig. 8; the program takes into account all the factors that affect the detector counts, including X-ray energy, degree of polarization, distances, detector acceptance angle, density of air or helium in front of detector, Be window thickness and density, etc. The detector efficiency curve provided by the manufacturer was used to simulate the response of the fluorescence detector. The simulated spectrum was compared with the experimental spectrum. The only adjustable parameters were the specimen concentrations, which were adjusted until the spectra matched. The concentrations that make the simulated spectra agree with the measured spectra are then the calculated concentrations. In this fitting procedure, the spectra had to be normalized to account for different sample thickness. This was done by equating the simulated and experimental intensities obtained from an element of known concentration. Since the detector efficiency has a strong dependence on energy in the region below 3 keV, the Sn L peaks were used to normalize the spectrum instead of the Zr L peaks. The Monte Carlo computer simulations of the fluorescence process were run until at least 50 000 counts for the thin foils were obtained in all the channels between 0 and 9 keV. After 20 000–30 000 counts per channel, no difference in the simulated spectra was observed. Therefore, the statistics of the simulated spectra are good enough to compare with the experimental data.

By first performing this simulation on the standards, we can verify that the simulation and fitting procedure

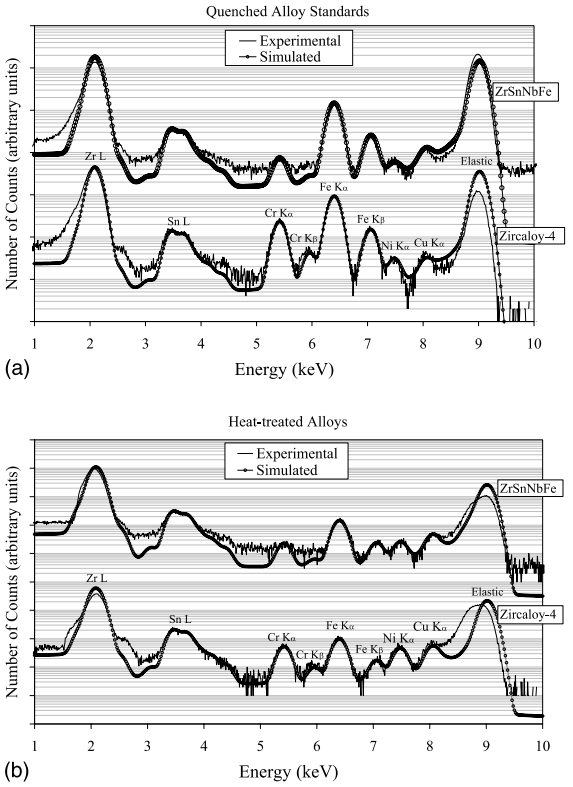

Fig. 9. X-ray fluorescence spectra of (a) quenched Zircaloy-4 and quenched ZrSnNbFe standards (measures and simulated by Monte Carlo program using the values in Table 1) and (b) α-Zr matrix in heat-treated Zircaloy-4 and ZrSnNbFe alloy (measured and simulated with Monte Carlo program using the values in Table 2). The vertical scale is logarithmic.

reproduce the known compositions. Fig. 9(a) shows the measured and simulated spectra for quenched Zircaloy-4 and the quenched ZrSnNbFe alloy. The simulated lines for the standards were generated using the values independently measured (and shown in Table 1), with no other adjustable parameters. The agreement with the standards is excellent for both alloys, throughout the energy range studied. Small differences between calculated and measured spectra exist in the region of the elastic peak. The counts in the elastic peak depend on sample-to-detector distance, angular acceptance of the detector, thickness of the sample and polarization of the beam. Small variations in sample thickness and shape of the sample could affect the elastic peak, and therefore, the Cu and Ni concentrations (present as impurities in the alloy). Since the Fe and Cr K peaks are far from the elastic peak, these peaks are not affected. Other small differences in the mid-energy range in the ZrSnNbFe sample are caused by the smaller counting times in that sample than in the Zircaloy-4 sample.

The simulated and measured spectra from the heat-treated Zircaloy-4 and ZrSnNbFe samples is shown in Fig. 9(b). In this case, after normalizing to the Sn peak, the concentrations of Fe and Cr in the simulation were varied to obtain the best fit. The concentrations used to obtain the fit shown are shown in Table 2. The values required to match the observed values were 290 wt. ppm Fe, 270 wt. ppm Cr in Zircaloy-4 and 250 wt. ppm Fe for the ZrSnNbFe alloy. The uncertainty on the calculated concentrations that originates in the experimental noise, and obtained by fitting the upper and lower limits of the spectrum noise, is about 10 wt. ppm. Very good agreement is observed between measurement and simulation, throughout the whole energy range, as shown by the log scale of Fig. 9: both the shape and the intensity of the various peaks is reproduced quite well. The Cr concentrations reported for the MC simulation agree in height, but the background is quite high in that region. It is likely that a longer counting time would have eliminated this discrepancy.

4. Discussion

The present results can be better understood when compared with other measurements of the concentrations of alloying elements in Zr alloys. Several researchers have attempted to find the terminal solid solubility (TSS) curve of Fe and other alloying elements in α-Zr [15–17]. Such measurements are difficult to perform because of the very small solubility of Fe in α-Zr, and have yielded values of Fe TSS of a few wt. ppm at lower temperatures and about 100 wt. ppm near 800 °C [15,16]. Borrelly et al. [15] used thermoelectric power method and Zou et al. [16] used secondary ion mass spectrometry technique to determine the solubility limits of Fe in α-Zr at 790 °C as ~100 wt. ppm. Although their results are in good agreement at high temperatures (790–830 °C), at lower temperatures (500–750 °C), Zou found lower Fe concentrations than Borrelly. While Borrelly measured Fe TSS values of about 6 and 0.6 wt. ppm at 600 and 500 °C, Zou measured those as 3 and 1 wt. ppm. Charquet et al. [17] measured the solubility of both Fe and Cr in a Zr–1.4%Sn–0.1%O alloy by individually adding Fe and Cr to the alloy, and found a maximum solubility in the α-phase of 120 wt. ppm Fe at 820 °C and 200 wt. ppm Cr at 860 °C, respectively. By adding both Fe and Cr with a Fe/Cr ratio of 2 to an oxygen free Zr–Sn alloy, the maximum solubility was determined to be 150 wt. ppm at 810 °C.

Another technique to measure the concentration of transition elements in the matrix of Zr-based alloys is atom probe microanalysis. This technique can be used to measure the matrix composition of the alloy directly. Wadman and Andren [18,19] used this technique to

study the concentrations of alloying elements in Zr alloys. They found the concentration of Fe, and Cr in the matrix of 'standard variant' Zircaloy-4 to be about 10% of the overall concentration of these elements in the alloy (110–220 wt. ppm of Fe, 90–140 wt. ppm of Cr) [19]. This standard variant was reported as having been annealed to an annealing parameter of $10^{-13.35}$ h but with $Q/R = 31,700$ K as opposed to 40 000 K, as in the present study. Wadman and Andren also report values for Zircaloy-2 of Fe = 190 wt. ppm, Cr = 70 wt. ppm, and Ni = 180 wt. ppm [19]. In a previous publication Wadman et al. had found matrix values for Fe and Cr in Zircaloy-4 that they later judged to be anomalous [19] of 400 and 100 wt. ppm [18]. In these measurements they had to compensate for the preferential field evaporation of Zr ions by normalizing the alloying element concentrations to the known Sn concentrations. This normalization therefore assumes that there is no preferential evaporation between of Sn compared to Fe or Cr. Kruger et al. [20] who used the same technique, found the concentrations of Fe, Cr and Ni in Zircaloy-2 alloy matrix to be much lower: Fe = 66 wt. ppm, Cr = 61 wt. ppm and Ni = 85 wt. ppm.

More recently, Li et al. [21] used an electrochemical method in which they preferentially dissolved the second phase particles and measured the concentrations of Fe and Cr in solution in Zircaloy-4, after various heat treatments. For the longest heat treatment they used (650 °C for 2 h followed by 470 °C for 4 h, CAP = 3×10^{-19} h) they found the concentrations of Fe and Cr in the α-Zr matrix to be 154 and 163 wt. ppm, respectively.

Thus there is a range of measurements of the alloying element content in the matrix of Zr alloys, obtained by different techniques, most of which are in the 100–400 wt. ppm range. Clearly some of these variations could be caused by specific heat treatments, by different techniques and/or analysis methods or even statistical variation. Taken as a whole, it is clear that these previous measurements [18–21] of transition alloys in the matrix of Zr alloys, as well as the measurements reported in the present work, find concentration values that are consistently higher than the TSS values of alloying elements in pure Zr (the TSS of Fe and Cr in pure Zr is reported on the order of ppm or less at equilibrium in the temperatures below 300 °C). There are physical reasons to believe that the actual measured concentration of these elements in Zr alloys, such as Zircaloy-4 and ZrSnNbFe, would be higher:

(1) The equilibrium TSS of Fe and Cr in a multicomponent system such as Zircaloy-4 (Zr–Sn–Fe–Cr–O–C–H, etc.) is likely higher than that of the same elements in pure Zr. For example, the results of Charquet et al. [17] mentioned above show a higher concentration of Fe and Cr in the matrix of Zr–Sn–O–Fe–Cr alloys than in the binary or ternary Zr–Fe–Cr alloys.

(2) As a result of the manufacturing process, the industrial alloys have a concentration of lattice defects such as dislocations, stacking faults and grain boundaries, with which the alloying elements can be associated, thus remaining 'suspended' in solution, neither precipitating, nor being in perfect substitutional or interstitial solid solution. Zou et al. [34] showed, for example, that Fe interacts preferentially with interfaces in annealed Zr alloys and de Carlan et al. showed it interacts with dislocation loops [6].

(3) At the end of the thermo mechanical processing, the alloys could be in a non-equilibrium state, or in a metastable equilibrium, simply because not enough annealing time has been given at the end of the processing route used to reach the most stable state. Such an approach to equilibrium depends not only on the mobility of the atoms concerned, but also on the driving forces for the reactions in question. For example, although the solid solubility of Sn at low temperatures in α-Zr is very small [35], higher Sn concentrations (on the order of 1.5 wt%) are commonly found in Zr alloys, a factor commonly attributed to the low mobility of Sn in Zr [35,36].

The factors 1–3 listed above would cause the measured concentration of Fe in the matrix to be higher than the TSS measured in pure Zr. By annealing both alloys, we minimize the impact of cause #3, but the other two causes likely influence the amount of alloying elements measured by the synchrotron beam (or by any other technique).

This discussion indicates that a clear definition of what is meant by 'Fe in solution in the alpha phase' is necessary for meaningful experiments to be performed. There are the various chemical and physical states that can be assumed by alloying elements such as Fe in the alloy. Following the arguments presented in Section 3.3.1, if we assume that we can eliminate the contributions to the measured signal from any precipitates with a diameter bigger than 80 nm, and since we have estimated that the probability is quite low that precipitates below 80 nm are intersected by the beam, then in the present experiment the individual contributions to the measured Fe signal from the matrix come from three different Fe populations:

(a) Fe atoms associated with lattice defects such as dislocations and grain boundaries.
(b) Fe atoms in the alpha-Zr matrix but chemically attached to other alloying elements in solid solution, such as Sn, or O.
(c) Fe atoms in true solid solution in the alpha-Zr matrix.

The experiment cannot distinguish between these three distinct possibilities. The interest of measurements such as we have performed here is in estimating the amount of alloying elements that could be immediately

available to affect microstructural evolution of the alloy. The current measurements indicate a greater availability of Fe and other alloying elements, to cause effects such as changing the vacancy migration energy [37], helping nucleate dislocation loops [6] or changing the diffusion parameters of other alloying elements [30] than would be estimated from straight thermodynamic considerations of binary alloys. The high concentrations of alloying elements suggest that these effects could happen without taking recourse in the Fe tied up in precipitates. The actual amount of Fe available to cause microstructural evolution would depend on the binding energy between the other alloying elements and Fe (population b) and between extended defects and Fe (population a), but the overall results of several techniques over the years indicate that this amount could be in the 100s of wt. ppm, and thus, significantly higher than the thermodynamic solid solubility in pure Zr.

5. Conclusion

We have used a synchrotron X-ray fluorescence microprobe to measure the concentrations of alloying elements in the matrix of Zr alloys. We used Monte Carlo simulation of the fluorescence process to quantify the alloying element concentration. The main results are as follows:

- The technique was well calibrated by performing measurements in known standards ranging from quenched alloys to nominally pure and simulating those with a Monte Carlo program. The agreement between the measured values and the bulk concentrations of these alloys, as measured by the overall fit of the full fluorescence spectrum was excellent.
- We show that with our method the minimum detectable precipitate size is 80 nm, and that this represents a small bias in the determination of alloying element concentration.
- We measured the insoluble alloying elements content in the matrix of Zircaloy-4 annealed to at 705 °C for 125 h ($CAP = 2.1 \times 10^{-16}$ h) and in the matrix of ZrSnNbFe (with a composition similar to ZIRLO) alloy annealed at 710 °C for 92 h. We find that the concentrations are in Zircaloy-4, Fe = 290 wt. ppm, Cr = 270 wt. ppm and in ZrSnNbFe, Fe = 250 wt. ppm.
- The high concentration of these transition alloying elements in the matrix as compared to the TSS in the pure metal could be attributed to several factors, including a higher TSS in the alloy as compared to the pure metal, the stabilization of alloying elements in solution by interaction with lattice defects, and the possibility that the alloys are not fully in equilibrium.

These results suggest that more alloying elements (in particular Fe) could be available to affect microstructural evolution during irradiation, than what would be estimated from straight solubility analyses of binary alloys.

Acknowledgements

Thanks are due to Ken Erwin and Sarah Jurgensmeier for their help with data collection. The authors would like to thank R.B. Adamson at GE, R.J. Comstock from Westinghouse, and G.P. Sabol, formerly from Westinghouse, for furnishing the samples used in this study. We are very grateful to L. Vincze for furnishing us with the copy of his program MSIM5D and for helping us set it up for our purposes.

Use of the Advanced Photon Source was supported by the US Department of Energy, Basic Energy Sciences, Office of Science, under Contract No. W-31-109-Eng-38. This research was sponsored by the Department of Energy, Nuclear Engineering Education and Research (DOE-NEER) program, under grant numbers DE-FG07-98ID 13637 and DE-FG07-01ID14115.

References

[1] C. Lemaignan, A.T. Motta, in: B.R.T. Frost (Ed.), Nuclear Materials, Materials Science and Technology, A Comprehensive Treatment, vol. 10B, VCH, New York, 1994, p. 1.
[2] D.F. Taylor, J. Nucl. Mater. 277 (2000) 295.
[3] B. Cheng, R.B. Adamson, in: Zirconium in the Nuclear Industry: 7th International Symposium, in: ASTM STP 939, 1987, p. 387.
[4] K. Ogata, in: Zirconium in the Nuclear Industry: 8th International Symposium, in: ASTM STP 1023, 1989, p. 346.
[5] C.T. Wang, C.M. Eucken, R.A. Graham, in: Zirconium in the Nuclear Industry: 9th International Symposium, in: ASTM STP 1132, 1991, p. 319.
[6] Y. de Carlan, C. Regnard, M. Griffiths, D. Gilbon, C. Lemaignan, in: Zirconium in the Nuclear Industry: 11th International Symposium, in: ASTM STP 1295, 1996, p. 638.
[7] G.M. Hood, R.J. Schultz, in: Zirconium in the Nuclear Industry: 8th International Symposium, in: ASTM STP 1023, 1989, p. 435.
[8] H. Zou, G.M. Hood, J.A. Roy, R.H. Packwood, J. Nucl. Mater. 245 (1997) 248.
[9] G.M. Hood, R.J. Schultz, N. Matsuura, J. Nucl. Mater. 226 (1995) 260.
[10] D. Pecheur, F. Lefebvre, A.T. Motta, C. Lemaignan, D. Charquet, in: Zirconium in the Nuclear Industry: 10th International Symposium, in: ASTM STP 1245, 1994, p. 687.
[11] D. Pecheur, F. Lefebvre, A.T. Motta, C. Lemaignan, J.-F. Wadier, J. Nucl. Mater. 189 (1992) 318.

[12] F. Garzarolli, W. Goll, A. Seibold, I. Ray, in: Zirconium in the Nuclear Industry: 11th International Symposium, in: ASTM STP 1295, 1996, p. 541.
[13] D. Charquet, in: Zirconium in the Nuclear Industry: 12th International Symposium, in: ASTM STP 1354, 2000, p. 3.
[14] O. Delaire, K.T. Erwin, A.T. Motta, R.C. Birtcher, J. Maser, B. Lai, in: Proceedings of ICONE-8: 8th International Conference on Nuclear Engineering, ASME, Baltimore, MD, USA, 2000, p. 595.
[15] R. Borrelly, P. Merle, L. Adami, J. Nucl. Mater. 170 (1990) 147.
[16] H. Zou, G.M. Hood, J.A. Roy, R.J. Schultz, J.A. Jackman, J. Nucl. Mater. 210 (1994) 239.
[17] D. Charquet, R. Hahn, E. Ortlieb, J.-P. Gros, J.-F. Wadier, in: Zirconium in the Nuclear Industry: 8th International Symposium, in: ASTM STP 1023, 1989, p. 405.
[18] B. Wadman, H.-O. Andren, in: Zirconium in the Nuclear Industry: 8th International Symposium, in: ASTM STP 1023, 1989, p. 423.
[19] B. Wadman, H.-O. Andren, in: Zirconium in the Nuclear Industry: 9th International Symposium, in: ASTM STP 1132, Kobe, Japan, 1991, p. 461.
[20] R.M. Kruger, R.B. Adamson, S.S. Brenner, J. Nucl. Mater. 189 (1992) 193.
[21] C. Li, B. Zhou, W. Zhao, P. Li, Q. Peng, J. Nucl. Mater. 304 (2002) 134.
[22] F. Adams, K. Janssens, A. Snigiev, J. Anal. At. Spectrom. 13 (1998) 319.
[23] Z.W. Chen, D.B. Wittry, J. Appl. Phys. 84 (1998) 1064.
[24] O. Delaire, M.Sc. thesis; in Nuclear Engineering, Pennsylvania State University, University Park, 2000.
[25] A.T. Motta, K.T. Erwin, O. Delaire, R.C. Birtcher, Y. Chu, J. Maser, D.C.Mancini, B. Lai, in: Zirconium in the Nuclear Industry: 13th International Symposium, in: ASTM STP 1423, Annecy, France, 2001, p. 59.
[26] J.P. Gros, J.F. Wadier, J. Nucl. Mater. 172 (1990) 85.
[27] G.P. Sabol, R.J. Comstock, R.A. Weiner, P. Larouere, R.N. Stanutz, in: Zr in the Nuclear Industry: 10th ASTM International Symposium, in: ASTM STP1245, Baltimore, 1994, p. 724.
[28] J. Wang, A.T. Motta, R.J. Comstock, unpublished research, 2000.
[29] C. Regnard, Etude Microstructurale de L'alliage Y15, Centre d'Etudes Nucleaires de Grenoble, Grenoble Note Technique DRN/SECC 50/90, 1990.
[30] G.M. Hood, H. Zou, R.J. Schultz, J.A. Roy, J.A. Jackman, J. Nucl. Mater. 189 (1992) 226.
[31] L. Vincze, K. Janssens, F. Adams, Spectrochim. Acta 48B (1993) 553.
[32] L. Vincze, K. Janssens, F. Adams, M.L. Rivers, K.W. Jones, Spectrochim. Acta 50B (1995) 127.
[33] L. Vincze, K. Janssens, F. Adams, K.W. Jones, Spectrochim. Acta Part B 50 (1995) 1481.
[34] H. Zou, G.M. Hood, J.A. Roy, R.H. Packwood, V. Weatherall, J. Nucl. Mater. 208 (1994) 159.
[35] J.P. Abriata, J.C. Bolcich, D. Arias, Bull. Alloy Phase Diagrams 4 (1983) 147.
[36] G.J.C. Carpenter, E.F. Ibrahim, J.F. Watters, J. Nucl. Mater. 102 (1981) 280.
[37] A.D. King, G.M. Hood, R.A. Holt, J. Nucl. Mater. 185 (1991) 174.